New halogen-bonded complexes of diiodine with 1,3,5-triaza-7-phosphaadamantane chalcogenides: a structural and computational investigation

PORTLOCK, Gemma, GREWAL, Karmjit, SAUNDERS, Matthew, TIZZARD, Graham J, COLES, Simon J, ALLEN, David W, HAMILTON, Alex and BRICKLEBANK, Neil <http://orcid.org/0000-0002-1614-2260>

Journal of Molecular Structure 1349 (2026) 143762

Contents lists available at ScienceDirect

Journal of Molecular Structure

journal homepage: www.elsevier.com/locate/molstr

New halogen-bonded complexes of diiodine with 1,3,5-triaza-7-phosphaadamantane chalcogenides: a structural and computational investigation

Gemma Portlock [a,1], Karmjit S. Grewal [a], Matthew Saunders [a], Graham J. Tizzard [c], Simon J. Coles [c], David W. Allen [a], Alex Hamilton [a,b,*], Neil Bricklebank [a,*]

[a] Biomolecular Sciences Research Centre, Sheffield Hallam University, Sheffield S1 1WB, United Kingdom
[b] School of Chemical and Physical Sciences, Victoria University of Wellington, New Zealand
[c] UK National Crystallography Service, Chemistry, Highfield Campus, Southampton SO17 1BJ, United Kingdom

ARTICLE INFO

Keywords:
Halogen bonding
Iodine
1,3,5-triaza-7-phosphaadamantane-7-oxide
1,3,5-triaza-7-phosphaadamantane-7-sulfide
Crystal structure
Computational methods

ABSTRACT

Whilst the coordination chemistry of 1,3,5-triaza-7-phosphaadamantane-7oxide (PTA=O) and -sulfide (PTA=S) towards transition metals is widely established, examples involving bonding to main-group elements such as halogens are relatively rare. In the presented work, the interaction of PTA=O and PTA=S with diiodine has been studied in solution and solid state. UV-visible spectroscopy indicates that in the solution phase iodine bonds with PTA=O *via* a nitrogen whereas with PTA=S the iodine bonds to the donor ligand *via* the sulfur. In contrast, crystallographic studies of the complexes show that in the solid state the diiodine interacts with a nitrogen atom of the adamantane cage in both PTA=O.I_2 and PTA=S.I_2, with near linear N-I-I units, and both compounds are halogen-bonded charge-transfer adducts. Contributions to crystal packing have been delineated through Hirshfeld surface analysis. The nature of the charge-transfer interaction in both compounds has been investigated by computational methods with DLPNO-CCSD(T), and further wavefunction analysis techniques.

1. Introduction

Research into the nature of halogen bonding has transformed this intermolecular interaction from an interesting curiosity to an important aspect of supramolecular chemistry and crystal engineering which is recognised as playing crucial roles in biological and materials science [1,2]. Most recent research into halogen bonding has focused on the interaction between organic halides and halogen bond acceptors [1,2]. However, the interaction between dihalogens and interhalogens with electron donors, known by various terms including charge-transfer and donor-acceptor interactions, has been known for over 150 years and is now recognised as being part of the wider family of halogen-bonding interactions [3] and continues to attract attention [4].

The cage-like tertiary phosphine, 1,3,5-triaza-7-phosphaadamantane (PTA), together with its oxide (PTA=O) and sulfide (PTA=S) derivatives (Scheme 1), are important ligands in organometallic chemistry [5–7], not least because, unlike most other tertiaryphosphines, PTA combines aqueous solubility with chemical and thermal stability and low steric requirements. Complexes of these ligands have been widely investigated for their applications in catalysis [8], and medicinal [9], chemistry. Furthermore, PTA, PTA=O and PTA=S offer multiple coordination sites, and have been investigated as building blocks in 3D metal frameworks and coordination polymers [10–15],

Although the coordination chemistry of PTA and its derivatives towards transition metals has been extensively investigated there are far fewer reports of their coordination to main group elements [16,17]. To the best of our knowledge there are no reports of the interaction of PTA derivatives with group 15 elements, other than the unusual Ru complex [RuCl{κ^3(*N,N,N*)-TP}PPh_3)(1-I_2-PTA)], which contains an I_2 molecule bonded to a N atom of a PTA ligand that is also coordinated to ruthenium [18]. This is in contrast to other tertiary phosphines and their chalcogenide derivatives, where dihalogen adducts have been the subject of much interest [3], and a wide variety of structures have been identified, ranging from simple adducts [19], to molecular species with bridging dihalogen molecules [20], and more complex supramolecular networks [21–24].

In an attempt to redress the paucity of studies on the complexes of PTA derivatives with heavier main group elements, we have used a

* Corresponding authors at: Biomolecular Sciences Research Centre, Sheffield Hallam University, Sheffield, S1 1WB, United Kingdom.
E-mail addresses: alex.hamilton@vuw.ac.nz (A. Hamilton), n.bricklebank@shu.ac.uk (N. Bricklebank).
[1] Present address: School of Ocean and Earth Science, National Oceanography Centre Southampton, University of Southampton, SO14 3ZH, United Kingdom

https://doi.org/10.1016/j.molstruc.2025.143762
Received 23 May 2025; Received in revised form 28 July 2025; Accepted 22 August 2025
Available online 23 August 2025

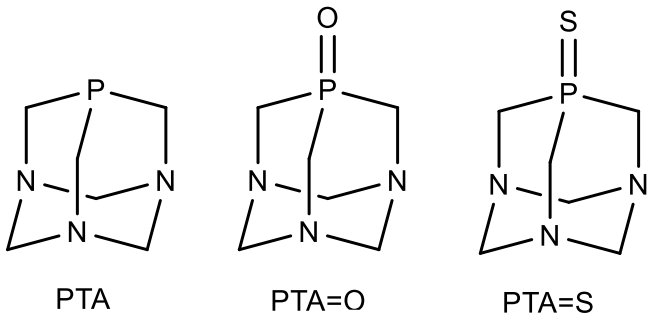

Scheme 1. 1,3,5-triaza-7-phosphaadamantane (PTA) and its chalcogen derivatives.

combination of experimental and computational methods to investigate the interaction of PTA=O and PTA=S with diiodine in solution and in the solid state.

2. Experimental

2.1. General information

Chemicals and solvents, including 1,3,5-triaza-7-phosphaadamantane, 1,3,5-triaza-7-phosphaadamantane-7-oxide and diiodine were purchased from Sigma-Aldrich or Fisher and used as received. 1,3,5-Triaza-7-phosphaadamantane-7-sulfide was prepared following published methods [25]. NMR spectra were recorded on a Brucker Advance III 400 MHz. Chemical shifts are reported in ppm. FT-IR spectra were recorded in the range 4000 - 400 cm^{-1} on a Brucker Alpha Platinum ATR spectrometer. Electrospray mass spectra were recorded on a Thermo-scientific Genesys 10S instrument. Elemental Analysis was completed by MEDAC Ltd. UV-visible spectra were recorded on a Thermo Scientific Genesys 105 spectrometer. UV-Vis titration experiments were completed on 0.32 mmol stock solutions of PTA=O, PTA=S and I_2 in dichloromethane.

2.2. Synthesis and characterisation

2.2.1. Synthesis of 1,3,5-triaza-7-phosphaadamantane-7-oxide diiodine, PTA=O.I_2 (1)

Diiodine (0.323 g, 0.001 mol) was dissolved in 20 ml dichloromethane. The solution was added to a sample of PTA=O (0.22 g, 0.001 mol), dissolved in 70 ml of dichloromethane. The mixture was left to stir for 2 h at room temperature under a nitrogen atmosphere. The solvent was allowed to evaporate slowly over a period of three days, producing a small crop of red/orange crystals.

Elemental Analysis: found: C, 17.01; H, 3.13; N 9.94. $C_6H_{12}N_3POI_2$ requires: C, 16.88; H, 2.83; N 9.84· **^{1}H NMR** (400 Hz, CD_2Cl_2) δ (ppm) 4.41(d, AB system, J_{AB} = 13 HZ, 3H, NCH_2N); 4.20 (d, AB system, J_{AB} = 13 Hz, 3H, NCH_2N); 3.97 (d, 2 J_{HP} = 9 Hz, 6H, PCH_2N); **^{31}P {^{1}H} NMR** (400 Hz, CD_2Cl_2) δ (ppm) -12.2; **MS (ESI)** m/z 196.1 $[PTA=O+Na]^+$, 174.0 $[PTA=O+H]^+$; **FT-IR** (ν_{max}/cm^{-1}): 2939(w), 2913 (w), 1439 (m), 1410 (m), 1355 (m), 1296 (m), 1229(m), 1178 (s) (ν P=O), 1158 (m), 1099 (m), 1086 (m), 969 (s), 948(m), 905 (m), 779 (m), 739 (m), 570 (s), 459 (m).

2.2.2. Synthesis of 1,3,5-triaza-7-phosphaadamantane-7-sulfide diiodine, PTA=S.I_2 (2)

PTA=S (0.0945 g, 0.5 mmol) was dissolved in the minimum amount of warm chloroform in a long cylindrical reaction tube and was covered with a layer of pentane (10 mL). Diiodine (0.127 g, 0.5 mmol) was dissolved in pentane (20 mL) and carefully layered on top of the PTA=S solution. The diiodine solution was then left to slowly diffuse into the PTA=S solution. After 2 weeks a homogenous red-brown coloured solution was observed together with a red/brown crystalline solid. The mother liquor was pipetted out of the tube and the crystal left to air dry, yielding 0.0177 g of product.

Elemental Analysis: found: C, 16.53; H, 2.76; N 9.32. $C_6H_{12}N_3PSI_2$ requires: C, 16.27; H, 2.73; N 9.48. **^{1}H NMR** (400 MHz, $CDCl_3$) δ (ppm) 4.45 (d, AB system, J_{AB} = 13 HZ, 3H, NCH_2N); 4.28 (d, AB system, J_{AB} = 13 Hz, 3H, NCH_2N); 4.01 (d, 2 J_{HP} = 6 Hz, 6H, PCH_2N); **^{31}P {^{1}H} NMR** (162 MHz, $CDCl_3$): δ (ppm); -20.4; **MS (ESI)** m/z: 189.9 $[PTA=S]^+$; **FT-IR** (ν_{max}/cm^{-1}): 2937 (w), 2899 (w), 1441 (w), 1419 (m), 1405 (m), 1358 (w), 1274 (m), 1244 (m), 1233 (w-m), 1089 (w-m), 1007 (m), 967 (m-s), 947 (s), 934 (m), 895 (w), 805 (w), 787 (w), 773 (w), 734 (s), 637 (m) (ν P=S), 596 (s), 571 (s), 448 (m).

2.3. X-ray crystallography

Single-crystal X-ray diffraction analyses of **1** and **2** were performed using a Rigaku FRE+ with VHF Varimax confocal mirrors, an AFC12 goniometer and HyPix 6000 hybrid pixel detector equipped with an Oxford Cryosystems low temperature apparatus operating at T = 100(2) K. CrysAlisPro [26] was used to record images, process all data and apply empirical absorption corrections. Unit cell parameters were refined against all data. The structures were solved by intrinsic phasing using SHELXT [27] and refined on Fo^2 by full-matrix least-squares refinements using SHELXL [28] as implemented within OLEX2 [29]. All non-hydrogen atoms were refined with anisotropic displacement parameters and hydrogen atoms were added at calculated positions and refined using a riding model with isotropic displacement parameters based on the equivalent isotropic displacement parameter (Ueq) of the parent atom. Figures were produced using OLEX2. Crystallographic parameters are reported in Table 1. The CIF files for the crystal structures of **1** and **2** have been deposited with the Cambridge Crystallographic Data Centre (CCDC) with the following deposition numbers,

Table 1
Crystallographic data for **1** and **2**.

Compound	1	2
Formula	$C_6H_{12}N_3OPI_2$	C6H12N3PSI2
$D_{calc.}$/ g cm^{-3}	2.540	2.463
μ/mm^{-1}	5.747	5.536
Formula Weight	426.96	443.02
Colour	orange	red
Shape	plate	block
Size/mm^3	0.07×0.04×0.01	0.05×0.05×0.03
T/K	100(2)	100(2)
Crystal System	orthorhombic	triclinic
Space Group	*Pbca*	P-1
a/Å	8.5600(2)	6.2461(2)
b/Å	8.6952(3)	8.2046(3)
c/Å	29.9956(8)	12.5978(5)
α/°	90	90.205(3)
β/°	90	94.103(3)
γ/°	90	111.836(3)
V/Å^3	2232.60(11)	597.42(4)
Z	8	2
Z'	1	1
Wavelength/Å	0.71075	0.71075
Radiation type	MoK_α	MoK_α
θ_{min}/°	2.716	2.676
θ_{max}/°	27.465	27.484
Measured Refl.	8146	6944
Independent Refl.	2548	2731
Reflections Used	2202	2558
R_{int}	0.0278	0.0158
Parameters	128	118
Restraints	7	0
Largest Peak	0.497	0.456
Deepest Hole	-0.498	-0.501
GooF	1.035	1.059
wR_2 (all data)	0.0489	0.0293
wR_2	0.0473	0.0289
R_1 (all data)	0.0268	0.0142
R_1	0.0203	0.0128

1977258-9 which contain the supplementary crystallographic data for this paper. These data can be obtained free of charge from The Cambridge Crystallographic Data Centre (https://www.ccdc.cam.ac.uk/).

2.4. Computational methods

All DFT optimisation calculations were performed at the RIJCOSX-PBE0/def2-TZVP level of theory [30–34], with dispersion interactions accounted for with Grimme's D3BJ correction [35]. All calculations were performed using the ORCA 6.0 computational software package [36]. Solvation correction was implemented with the SMD [37] model for dichloromethane, at the ωB97M-V/def2-qzvpp level of theory [38]. Graphical visualisation with Gabedit 2.4.8 [39] and Avogadro 1.9 [40]. Analytical frequencies were calculated for inclusion of the Zero Point Energy (ZPE) correction and entropic contributions to the free energy term (ΔG_{298K}), as well as confirming that all intermediates were true, with no imaginary modes. QTAIM and NCI analysis was performed using the Multiwfn software package [41].

Time-dependent density-functional theory (TD-DFT) calculations were performed at the ωB2GP-PLYP/def2-TZVPP level of theory [42], based on the gas phase RIJCOSX-PBE0/def2-TZVP geometries. The use of a long range corrected (LC) double hybrid method proved necessary for correct prediction of the intermolecular charge transfer halogen bonding interactions,.

To obtain a more accurate description of the energetics and analysis using the Local Energy Decomposition (LED) [43] scheme DLPNO-CCSD (T)/def2-QZVPP [46] calculations were performed on all structures. Due the interest in non-covalent interactions, the *tight*-PNO settings were used, which has been shown to be within 0.5-1 kcal mol^{-1} of canonical CCSD(T) calculations [44], but with a significant reduction in cost.

3. Results and discussion

Reaction of PTA=O or PTA=S with one molar equivalent of diiodine in dichloromethane, chloroform, acetonitrile or DMSO results in an immediate colour change from colourless to orange/brown (Scheme 2), indicating the formation of charge-transfer complexes.

The reactions were monitored by UV-vis spectroscopy. The spectra of the parent PTA=O and PTA=S ligands in dichloromethane show no bands above the solvent cut-off at 235 nm. The addition of one mole equivalent of diiodine to the PTA=O or PTA=S solutions results in a peak at 255 nm or 270 nm, respectively (Fig. 1), characteristic of charge-transfer complexes [45,46]. If the mole ratio of diiodine to PTA=O or PTA=S is increased, a broad band with a λ_{max} of 500 nm appears in the spectra which is characteristic of free I_2 [47]. Time-dependent density-functional theory (TD-DFT) calculations, with the range-separated double-hybrid functional ωB2GP-PLYP were used to predict UV-visible spectra for each binding adduct of PTA=O.I_2 and PTA=S.I_2 (Fig. 1) [42]. The calculated spectra for PTA=O.I_2 adducts have distinct peaks at 255 nm for N-bound and 229 nm for O-bound, whereas for PTA=S.I_2 the calculated spectra show peaks at 259 nm for N-bound and 268 nm for S-bound. The calculations are in excellent agreement with the experimental data suggesting that in the solution phase I_2 binds to PTA=O *via* the nitrogen and with PTA=S the I_2 binds *via* the sulfur.

The ^{31}P NMR spectrum for PTA=O shows a single peak at δ = -13.6 ppm in CD_2Cl_2. Progressive addition of up to four molar equivalents of I_2 results in a shift in the phosphorus signal to -12.2 ppm, the slight shift being indicative of weak interaction between the iodine and the phosphoryl group. The ^{31}P NMR of PTA=S has a single peak at -22.9 ppm and addition of I_2 results in a shift to -20.4 ppm. The downfield shift of the phosphorus NMR signals indicates that the iodine is interacting with the sulfur in the solution phase.

The infrared spectra of solid samples of **1** and **2** display ν(P=O) and ν(P=S) stretches at 1167 cm^{-1} and 629 cm^{-1} respectively, which are very similar to those observed in the parent ligands [25], and other main group element *N*-bound complexes [16,17].

3.1. Crystallographic studies

In order to establish the nature of the interaction between diiodine

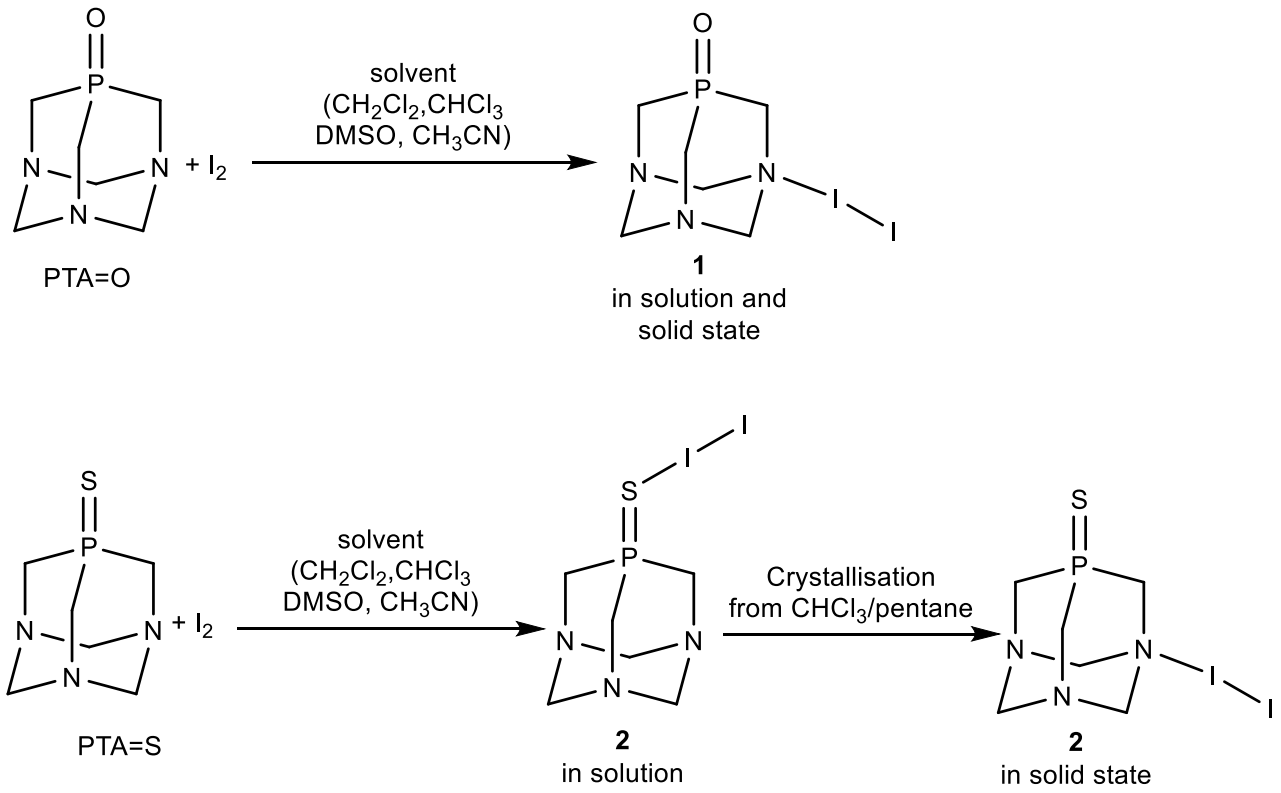

Scheme 2. Schematic summary of synthesis employed in this study.

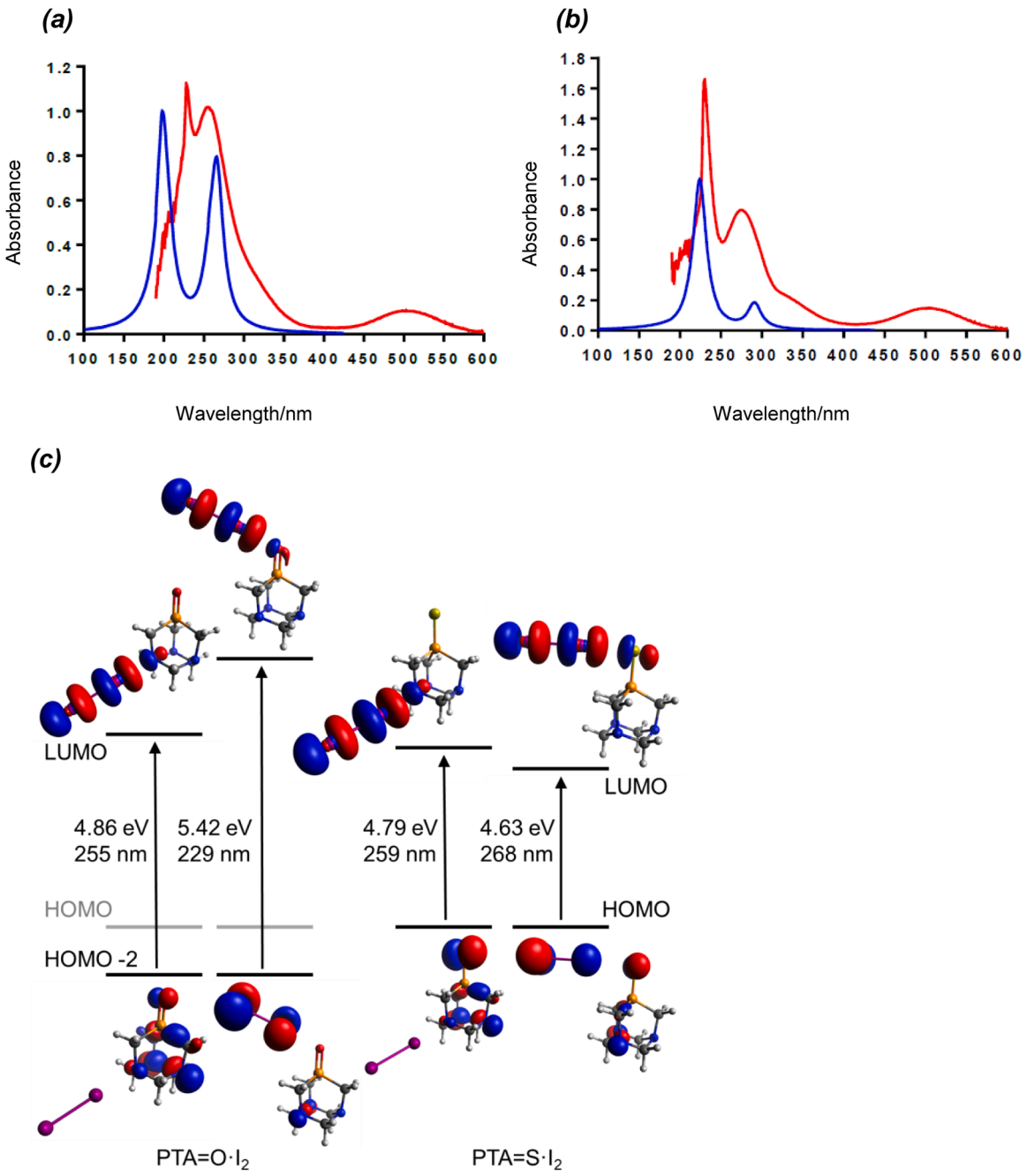

Fig. 1. *(a)* Experimental (red line) and calculated (blue line) UV-visible spectra of PTA=O and I_2 and *(b)* PTA=S and I_2 in dichloromethane. *(c)* Calculated excitations of PTA=O.I_2 and PTA=S.I_2 using TDDFT calculations at the ωB97X-V/def2-QZVPP level of theory.

with PTA=O and PTA=S, crystals of PTA=O.I_2 (**1**) and PTA=S.I_2 (**2**) were grown for X-ray analysis. Based on the initial solution investigations described above, our working hypothesis was that in **1** the iodine would bond with nitrogen of the PTA=O, whereas in **2** the iodine would interact with the sulfur of PTA=S. Single crystals of **1** were obtained by slow evaporation of a CH_2Cl_2 solution whereas those of **2** were obtained by diffusion of pentane into a solution of **2** dissolved in CH_2Cl_2. As expected, the structure of **1** (Fig. 2) is a charge-transfer complex in which the iodine interacts with one of the N atoms of the 1,3,5-triaza-7-phosphaadamantane cage. Previous studies of the interaction of diiodine with molecules that contain both nitrogen and oxygen electron donor sites show that the iodine bonds preferentially with the nitrogen atom [3,48]. There is some disorder in the I_2 moiety, with the terminal iodine atom occupying two positions, I2a and I2b, in a 76:24 ratio.

To our surprise, the crystal structure of **2** (Fig. 2) revealed a charge-transfer complex in which the iodine also bonds to a nitrogen rather than the sulfur, indeed there are no close contacts between an iodine or the sulfur atoms in **2**. This result is in contrast to previous studies of diiodine adducts of ligands containing sulfur and nitrogen electron donors atoms in which the diiodine prefers to bond with the sulfur. Moreover, the sulfur is in a lower hybridisation state (sp^2 compared with sp^3 for the nitrogen) and has a greater electron density than the nitrogen atoms, which should favour a S…I interaction over a N….I interaction [48].

Selected bond lengths and angles in **1** and **2** are reported in Table 2. The disorder in the I_2 component of **1** is manifested in two N-I-I angles and I-I bond lengths. The N-I-I bond angles in both compounds are close to linear (Table 2), and the N-I and I-I bond lengths are typical of those of similar adducts. Of greatest relevance to this work is [RuCl{κ^3(*N,N,N*)-

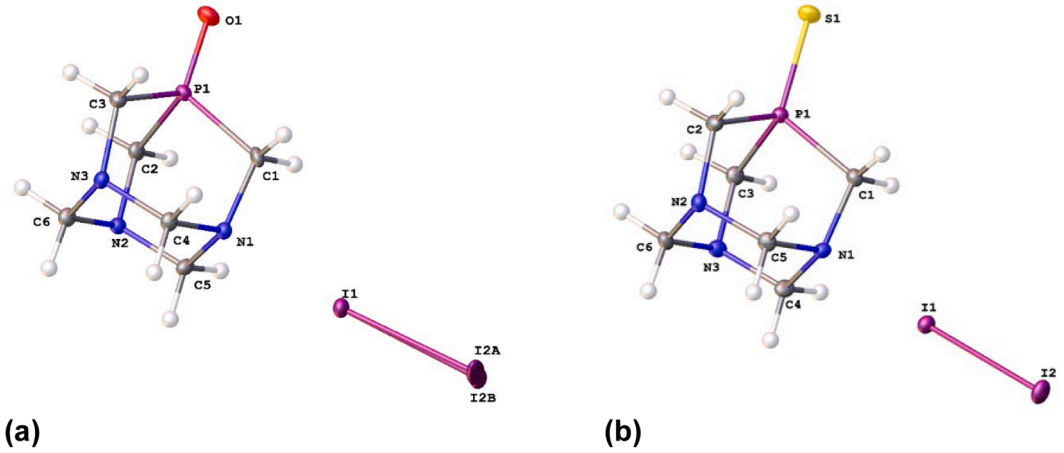

Fig. 2. Molecular structures of (a) PTA=O.I_2 (1), and (b) PTA=S.I_2 (2), showing atom numbering.

Table 2
Bond lengths (Å) and angles (°) in **1** and **2**.

1			
N1-I1	2.566(3)	N1-C4	1.489(3)
I1-I2A	2.7631(18)	N1-C5	1.485(3)
I1-I2B	2.735(6)	N2-C2	1.482(3)
P1-O1	1.487(2)	N2-C5	1.460(3)
P1-C1	1.814(3)	N2-C6	1.464(3)
P1-C2	1.813(3)	N3-C3	1.480(3)
P1-C3	1.815(3)	N3-C4	1.460(3)
N1-C1	1.481(3)	N3-C6	1.474(3)
N1-I1-I2a	171.73(8)	C5-N2-C6	108.7(2)
N1-I1-I2b	172.6(3)	C6-N2-C2	111.1(2)
O1-P1-C1	116.40(12)	C4-N3-C3	112.0(2)
O1-P1-C2	117.76(11)	C4-N3-C6	108.8(2)
O1-P1-C3	117.76(11)	C6-N3-C3	111.1(2)
C1-P1-C3	100.51(12)	N1-C1-P1	110.25(19)
C2-P1-C1	100.46(12)	N2-C2-P1	109.72(17)
C2-P1-C3	100.88(13)	N3-C3-P1	109.71(17)
C1-N1-C4	111.0(2)	N3-C4-N1	112.9(2)
C1-N1-C5	111.4(2)	N2-C5-N1	112.9(2)
C5-N1-C4	109.0(2)	N2-C6-N3	114.3(2)
C5-N2-C2	112.4(2)		
2			
N1-I1	2.5279(15)	N1 C5	1.487(2)
I1-I2	2.7772(2)	N2 C2	1.480(2)
S1 P1	1.9385(6)	N2 C5	1.458(2)
P1 C1	1.8231(18)	N2 C6	1.469(2)
P1 C2	1.8200(18)	N3 C3	1.478(2)
P1 C3	1.8311(17)	N3 C4	1.459(2)
N1 C1	1.484(2)	N3 C6	1.467(2)
N1 C4	1.493(2)		
N1-I1-I2	172.85(3)	C5-N2-C6	109.31(13)
C1 P1 S1	116.77(6)	C6-N2-C2	110.79(14)
C1 P1 C3	99.69(8)	C4-N3-C3	112.52(14)
C2 P1 S1	116.02(6)	C4-N3-C6	109.24(14)
C2-P1-C1	100.65(8)	C6-N3-C3	112.08(13)
C2-P1-C3	100.77(8)	N1-C1-P1	109.75(11)
C3-P1-S1	119.72(6)	N2-C2-P1	110.72(11)
C1-N1-C4	110.93(14)	N3-C3-P1	108.94(12)
C1-N1-C5	112.15(13)	N3-C4-N1	112.42(13)
C5-N1-C4	108.57(14)	N2-C5-N1	113.64(14)
C5-N2-C2	110.77(13)	N3-C6-N2	113.94(14)

TP}PPh_3)(1-I_2-PTA)] (**3**), which contains an I_2 molecule bonded to a N atom of a PTA ligand that is also coordinated to ruthenium [18], and the diiodine adduct of hexamethylenetetramine (**4**) [49]. The I-I bond lengths in **1** [2.7631(18) and 2.735(6) Å] and **2** [2.7772(2) Å] are longer than the I-I bond length of I_2 in the gas phase (2.677 Å) [50], or solid state (2.681 Å) [51], as expected for a charge transfer interaction. Furthermore, they are shorter than the I-I bond distance in **3** [2.8134(6) Å], but longer than that in **4** [2.439(8) Å]. Conversely, the N-I bonds in **1** [2.566(3) Å] and **2** 2.5279(15) Å] are slightly longer than that in **3** [2.422(6) Å], and shorter than that in **4** [2.439(8) Å]. There are no close inter- or intra-molecular interactions between the terminal iodine of the N…I-I moiety and other donor atoms. Therefore, following the classification of Pennington and coworkers [3], complexes **1** and **2** are 'simple adducts' and the bond parameters are consistent with a weak charge transfer interaction [52].

The P=O bond in **1** [1.487(2) Å] is slightly longer than that in PTA=O [1.476(2) Å] [47], but is comparable to the P=O bond length in *N*-bonded complexes of this ligand [17,18]. In contrast, the P=S bond length in **2** [1.9385(6) Å] is shorter than that in PTA=S [1.9572(4) Å] [25], but is also comparable to the P=S bond lengths in *N*-bonded complexes of this ligand [17].

3.2. Computational analysis

To gain a deeper insight into the nature of the halogen bonding interaction we turned to quantum chemical calculations. Halogen bonding is notoriously difficult to study using traditional Density Functional Theory (DFT) methods [53], and small adduct complexes are often studied with high level wavefunction methods [54]. Due to the size of the PTA adduct system we applied the locally correlated Domain-based Local Pair Natural Orbital CCSD(T) (DLPNO-CCSD(T)) method on the DFT optimised geometries. DLPNO-CCSD(T) is a near linear-scaling wavefunction method that approaches CCSD(T) accuracy at a significantly reduced computational cost [44]. DFT optimised geometries of both adducts **1** and **2** agree with the reported crystal structures (Fig. 2), showing preferential halogen bonding to the nitrogen of the PTA cage rather than the chalcogen. Relative free energies, based on the DLPNO-CCSD(T) electronic energies with DFT (PBE0-D3BJ/-def2-tzvp) solvation, thermal and entropic corrections are given in Table 3. The smaller energy difference for the sulfur complex has been further explored.

Local Energy Decomposition (LED) analysis has been applied to the DLPNO-CCSD(T) adduct interaction energies to decompose them into physically meaningful contributions. Detailed discussion of the LED scheme and its applications has been extensively discussed elsewhere [43]. Here we will only highlight the important aspects for our interests. The decomposed electronic contributions from the LED analysis are given in Table 3.

In the LED scheme the binding energy (ΔE_{bind}) between two molecular fragments can be expressed as the inter-fragment electronic

Table 3
DFT binding free energies (ΔG_{298K}) and LED-DLPNO-CCSD(T) contributions.

	ΔG_{298K}	ΔE_{bind}	$\Delta E_{geo\text{-}prep}$	ΔE_{int}	$\Delta E_{el\text{-}prep}$	E_{elstat}	E_{exch}	$\Delta E_{non\text{-}disp}$	E_{disp}	$\Delta E_{C\text{-}(T)}$	$E_{disp}/\Delta E_{int}$
1	-2.37	-9.60	3.75	-13.35	212.7	-176.4	-37.98	-0.81	-9.78	-1.07	0.733
1-O	0.78	-8.37	1.10	-9.47	110.0	-94.5	-18.80	1.49	-6.77	-0.91	0.715
2	-1.69	-9.32	3.13	-12.45	197.1	-162.5	-35.56	-0.91	-9.55	-1.03	0.767
2-S	0.89	-8.26	4.19	-12.45	250.7	-205.6	-45.60	-0.52	-9.52	-1.99	0.764

ΔG_{298K} of binding calculated at ωB97M-V/def2-qzvpp//PBE0-D3BJ/def2-tzvp, concentration corrected for 1:3 PTA=E:I_2 (E = O,S) ratio. ΔE terms calculated at DLPNO-CCSD(T)/ def2-qzvpp//PBE0-D3BJ/def2-tzvp. All energy values given in kcal mol^{-1}.

interaction term (ΔE_{int}) and a geometric preparation ($\Delta E_{geo\text{-}prep}$) term, eq (1). The $\Delta E_{geo\text{-}prep}$ term is an energy penalty for bringing the monomer components into the complex geometry. While the ΔE_{int} term describes the electronic features leading to the molecular interaction, which can be further decomposed into the constituent contributions; "electronic preparation" ($\Delta E_{el\text{-}prep}$), electronic interaction (E_{elint}), exchange energy (E_{exch}), dispersion energy (E_{disp}) and interaction energy from the triples correction ($E_{C\text{-}(T)}$), eq (2).

$$\Delta E_{bind} = \Delta E_{int} + \Delta E_{geo-prep} \quad (1)$$

$$\Delta E_{int} = \Delta E_{el-prep} + E_{elint} + E_{exch} + E_{disp} + E_{C-(T)} \quad (2)$$

with

$$\Delta E_{el-prep} = \Delta E^{HF}\ \mathrm{el-prep} + \Delta E^{C_{el-ph}}_{el-prep} \quad (3)$$

$$E_{elint} = E_{elstat} + E_{CT(X\rightarrow Y)} + E_{CT(X\leftarrow Y)} \quad (4)$$

$$E_{disp} = E^{disp}{}_{C\_SP} + E_{C-WP} \quad (5)$$

From the relative binding free energies (ΔG_{298K}) and LED analysis reported in Table 3 it is evident that, for both PTA=O and PTA=S cages, the I_2 preferentially binds to the nitrogen position in both systems. Based on the LED analysis, for PTA=O this preference is due to the significantly stronger electronic interaction energy (ΔE_{int}) overcoming the geometry preparation ($\Delta E_{geo\text{-}prep}$) penalty. Interestingly, for PTA=S, ΔE_{int} terms are equivalent while $\Delta E_{geo\text{-}prep}$ term determines the preference for binding to nitrogen, with a lower energy penalty for **2**. As discussed, the expected structure for the PTA=S-I_2 adduct was with binding *via* the sulfur, due to increased electron density, which is evident in the greater stabilisation in the E_{elstat} and E_{exch} terms. However, the $\Delta E_{el\text{-}prep}$ terms, which can be thought of as the energy investment to bring the fragments into the optimal electronic structure, is significantly greater for **2-S**, counteracting these effects.

The ratio $\mathbf{E_{disp}/\Delta E_{int}}$ gives a description of the importance of the dispersion term to the overall electronic interaction. A value greater than 1 identifies dispersion as the dominant interaction, a ratio less than 0.5 suggesting that non-dispersive contributions dominate. As shown in Table 3, for all structures, this value falls between 0.7 to 0.8, imply a balance of contributing facts, with PTA=S structures having a slightly greater dispersion dominance.

Quantum Theory of Atoms in Molecules (QTAIM) topological analysis of structures **1** and **2**, (Fig. 3) and the respective chalcogen-bonded adducts, have been performed to determine the line critical point (*lcp*) properties (Table 4) of the non-covalent interactions.

Analysis of the lcp properties for both **1** and **2** show very similar QTAIM characteristics. Line critical points having $\nabla^2\rho > 0$ but with H < 0, imply a strong closed shell interaction, characteristic of halogen bonding. Slight differences in ρ and H suggest a stronger halogen bonding interaction in **1** compared to **2**, in agreement with the calculated electronic interaction energies, ΔE_{int}.

The differences in lcp properties between **1** and **1-O**, are as expected, showing a stronger halogen interaction for **1**, greater values for ρ and H, with a concomitant weakening of the diiodine bond, with smaller values for ρ and H. The decrease in the value of $\nabla^2\rho$ for the I_2 bond suggests a more covalent/less ionic interaction and therefore a smaller charge

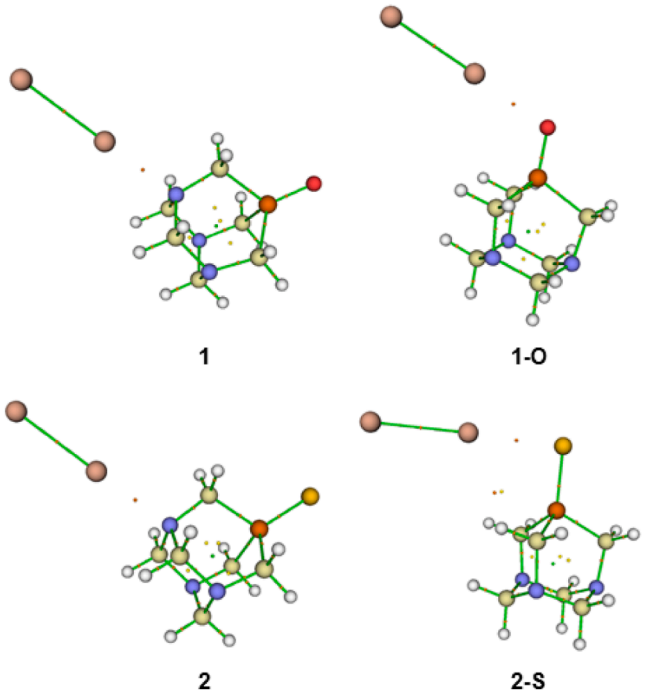

Fig. 3. DFT optimised structures (PBE0-D3BJ/def2-tzvp) for **1**(a), **1-O**(b), **2**(c) and **2-S**(d), showing line critical points (lcp) used in QTAIM analysis.

Table 4
QTAIM analysis and line critical point (lcp) characteristics.

	lcp	ρ	$\nabla^2\rho$	H	V	G
1	N···I	0.0478	0.0817	-0.0082	-0.0367	0.0286
	I···I	0.0589	0.0259	-0.0140	-0.0345	0.0205
1-O	O···I	0.0356	0.0983	-0.0026	-0.0298	0.0272
	I···I	0.0640	0.0203	-0.0168	-0.0388	0.0219
2	N···I	0.0459	0.0810	-0.0074	-0.0350	0.0276
	I···I	0.0607	0.0243	-0.0151	-0.0362	0.0212
2-S	S···I	0.0375	0.0606	-0.0045	-0.0242	0.0197
	I···I	0.0563	0.0328	-0.0124	-0.0331	0.0206
	H···I	0.0077	0.0228	0.0010	-0.0037	0.0047

Characteristics of LCP: the electron density(ρ), its Laplacian ($\nabla^2\rho$), the total electron energy density (*H*), and its components, the potential electron energy density (*V*), and the kinetic electron energy density (*G*).

transfer interaction in **1-O**. Interestingly, the lcp properties for **2** and **2-S** do not show the same trends. Compared to **2**, the halogen interaction in **2-S** has the expected lower ρ, in agreement with the nitrogen bound being the preferential interaction, a decrease in $\nabla^2\rho$ and a decrease in H. The decrease in $\nabla^2\rho$ suggests a slight increase in the covalency of this interaction. The diiodine interaction shows a decreased value of ρ, with an increased value for $\nabla^2\rho$ and a decrease in H. This suggests a weaker interaction, but with more covalent nature, presumably from an increase in charge transfer interaction for **2-S** compared to **2**, but countered by a steric interaction. Similar observations about the electronic interactions

were made in the LED analysis, Table 3, and are also highlighted by a 0.04 Å increase in the calculated diiodine bond length in **2-S**.

The relative energy differences between structures can also be accounted for in the QTAIM results. As previously mentioned, the binding free energies (ΔG_{298K}) shown in Table 3, are both in favour of the nitrogen-bound adducts. The smaller difference for the PTA=S adducts can be accounted for by the complex interplay between increased stabilising electronic parameters discussed in the LED and QTAIM analysis and the additional destabilising steric interactions observed between the -CH_2 moiety and the I_2. The H···I distance is 0.163 Å shorter in **2-S** (3.162 Å) compared to **1-O** (3.325 Å) and there is no equivalent lcp within the PTA=O system. From the DFT optimised structures the P-E-I angles for the chalcogen-bound structures are 116.5° and 91.4° for **1-O** and **2-S**, respectively. The smaller P-S-I angle, caused by the longer P-S bond compared to the P-O bond (1.96 Å to 1.49 Å, respectively) leads to a better orbital overlap in the HOMO (Fig. 4), and therefore the increased electronic stabilisation as previously discussed. The decreased P-S-I angle also brings the I_2 molecule into closer contact with the PTA cage, leading to the steric interactions mentioned.

Non-covalent interaction (NCI) analysis, using the reduced density gradient (RDG) *versus* sign(λ_2)ρ and the respective isosurface plots (Fig. 4) give another complementary method to analyse the non-covalent interactions of each structure [55]. Spikes of low density and low gradient lying at negative values correspond to stabilising interactions (halogen and hydrogen bonding), whilst spikes in the positive region correspond to steric effects. Spikes around zero correspond to weak van der Waals type interactions. All four plots of RDG *versus* sign (λ_2)ρ in Fig. 4 show spikes in the sign(λ_2)ρ region of +0.015 to +0.025. These correspond to the steric effects of the PTA cage structure, evident in the respective isosurface plots. Plots **a** and **c** have more prominent spikes at the -0.05 region, corresponding to more stabilising (*i.e.* stronger) halogen bonding. In the plots **b** and **d** the halogen to chalcogen bonding corresponds to the spikes around -0.04 and there are additional van der Waals interactions, both stabilising at -0.01 and sterically hindering in the region of +0.01.

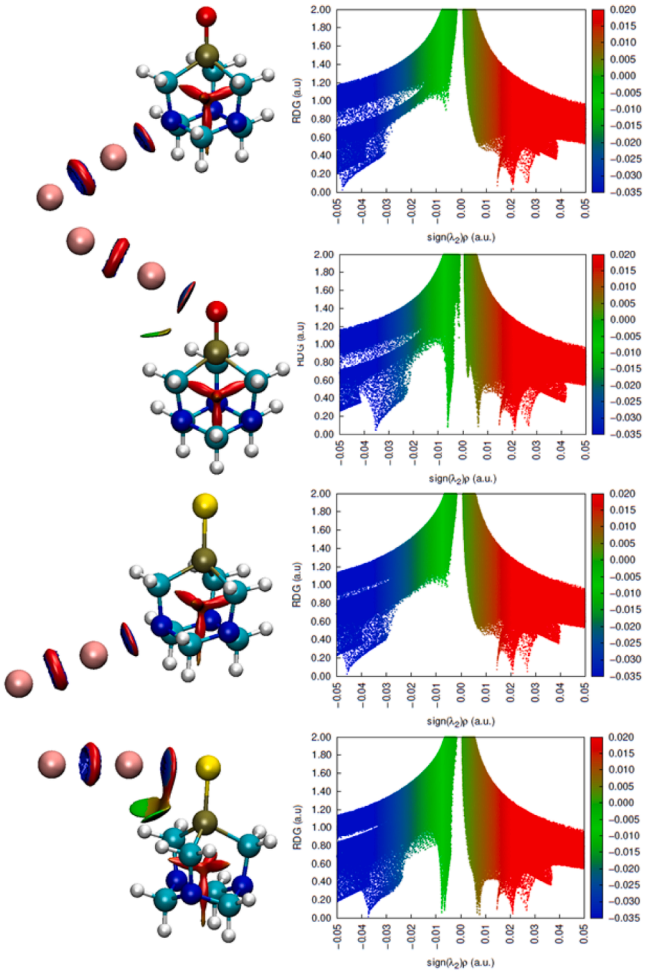

Fig. 4. DFT optimised structures (PBE0-D3BJ/def2-tzvp) for **1**(a), **1-O**(b), **2**(c) and **2-S**(d). Showing line critical points (lcp) used in QTAIM analysis and the corresponding non-covalent interaction (NCI) isosurface and RDG *vs* sign(λ_2)ρ scatterplots.

These additional interactions, in scatter plots **b** and **d**, are clearly evident in the respective structural isosurface plot, most prominently in plot **d**, corresponding to structure **2-S**. This visual inspection of NCI analysis gives further strength and evidence to previously discussed LED and QTAIM results.

The complex interplay between electronic and steric interactions leading to relatively small energy differences for the PTA=S adducts, explains why the expected halogen bonding interactions are not observed in the crystal structure, although evidence for them is seen in the solution phase, where the dynamic nature of the medium would influence behaviour.

To better understand the van der Waals (vdW) interactions in the solid state, Hirshfeld surface analysis was performed using the *CrystalExplorer21* package [56]. Fig. 5 shows the generated Hirshfeld surfaces mapped over d_{norm}, for **1** and **2**, highlighting the observed crystal packing close contacts. The d_{norm} mapped surface show shorter-than vdW contacts (red regions), normal vdW contacts (white regions), and longer-than vdW contacts (blue regions), for specific atom-to-atom interactions.

To further investigate the intermolecular interactions, two-dimensional fingerprint plots [57] were generated for **1** and **2**, as shown in Figs. 6 and 7 respectively. In both systems the *H··H* interactions have the greatest contribution to solid state packing, 47.3% and 37.9%, followed by the chalcogen (O and S) hydrogen interactions, 22.2% and 26.8%, respectively. The charge-transfer iodide interactions (*I··N*) make minimal contribution to the solid-state packing.

4. Conclusion

The facile reaction of PTA=O or PTA=S with an equimolar quantity of diiodine in dichloromethane yields the corresponding complexes, PTA=O.I_2 (**1**) and PTA=S.I_2 (**2**). Although numerous transition metal complexes of PTA and its derivatives have been reported, there are far fewer examples of these ligands bonding to main group elements [17, 18] and **1** and **2** are the first heavier main group element compounds of

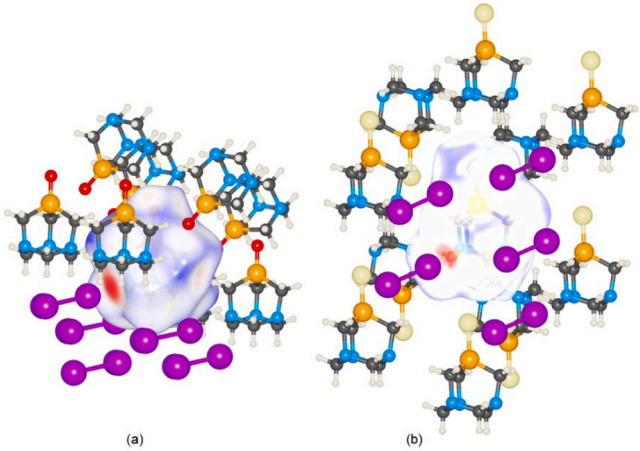

Fig. 5. Three-dimensional Hirshfeld surfaces for **1** (a) and **2** (b) mapped over d_{norm}.

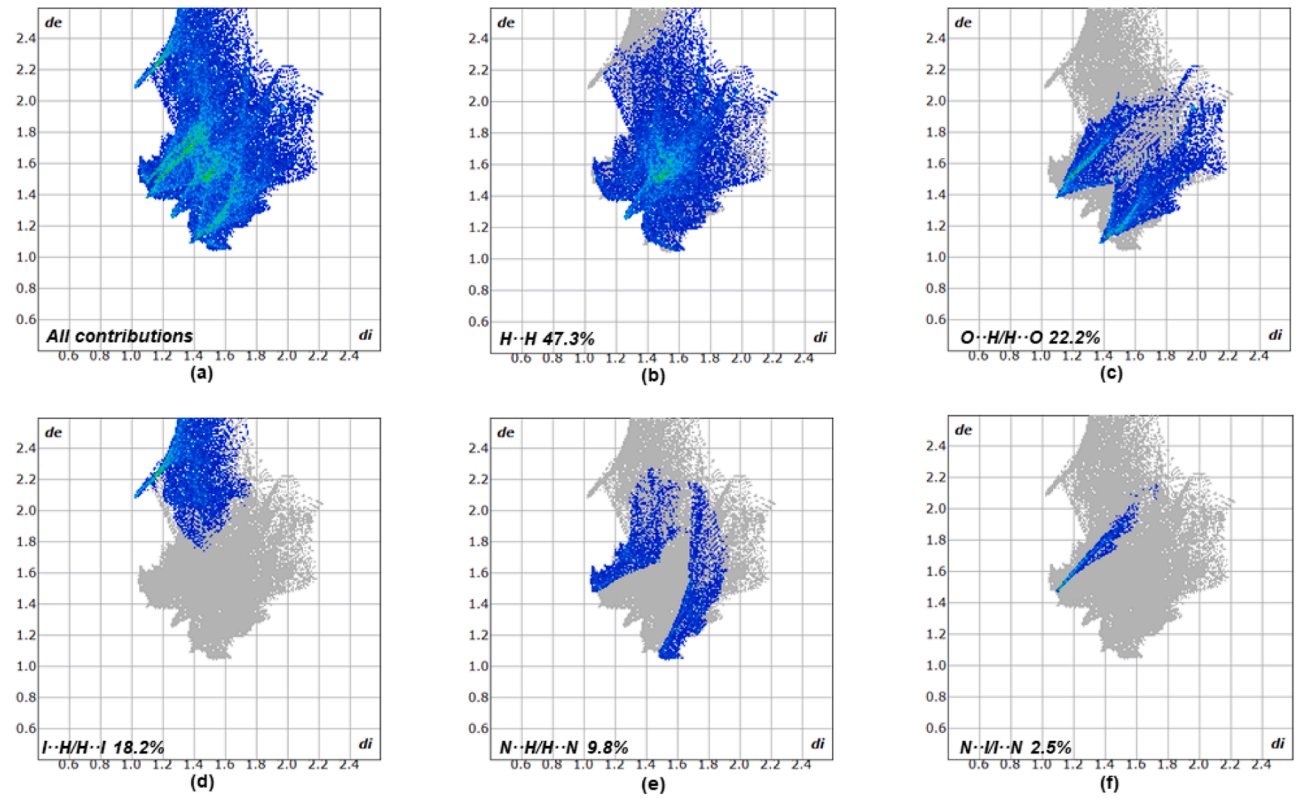

Fig. 6. Two-dimensional fingerprint plots for **1** showing (a) all contributions, and (b)–(f) delineated into contributions from other contacts (blue areas) [d_e and d_i represent the distances from a point on the Hirshfeld surface to the nearest atoms external and internal to the surface, respectively].

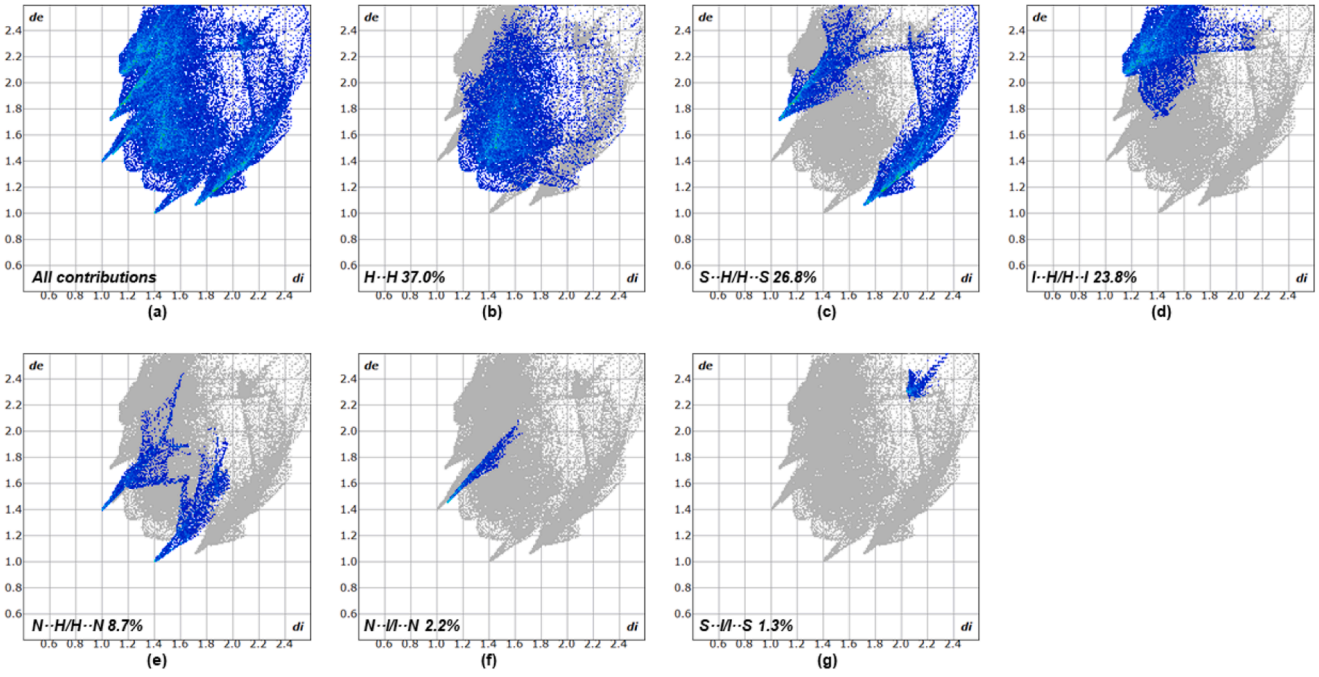

Fig. 7. Two-dimensional fingerprint plots for **2** showing (a) all contributions, and (b)–(g) delineated into contributions from other contacts (blue areas) [d_e and d_i represent the distances from a point on the Hirshfeld surface to the nearest atoms external and internal to the surface, respectively].

these important organophosphorus ligands. Furthermore, to the best of our knowledge, this work represents the first comprehensive investigation into the halogen bonding of diiodine with these compounds. In the PTA=O derivative **1**, the diiodine bonds to one of the nitrogen atoms of the triaza-adamantyl cage in both solution and in the crystalline states. Interestingly, the PTA=S derivative **2** is more dynamic, with evidence for binding *via* the sulfur in the solution phase and, unexpectedly, *via* the nitrogen in the solid state. In-depth computational analysis of the halogen bonding interactions, using Local Energy Decomposition on the DLPNO-CCSD(T) wavefunction, highlights the complex interplay

between steric and electronic factors which drive the observed binding. Quantum Topological (QTAIM), Non-Covalent Interaction (NCI) and Hirshfield analysis provide further support for these findings and help to rationalise the factors that influence the structure of these compound in the solid state.

Significant interest continues to be exhibited in the biomedical applications of iodine-containing compounds [58], and diiodine adducts of PTA derivatives are of potential interest as reagents in synthetic chemistry and as antimicrobial agents.

Funding sources

This research did not receive any specific grant from funding agencies in the public, commercial, or not-for-profit sectors.

CRediT authorship contribution statement

Gemma Portlock: Investigation. **Karmjit S. Grewal:** Investigation. **Matthew Saunders:** Investigation. **Graham J. Tizzard:** Writing – review & editing, Writing – original draft, Investigation, Formal analysis. **Simon J. Coles:** Investigation. **David W. Allen:** Writing – original draft, Conceptualization. **Alex Hamilton:** Writing – review & editing, Writing – original draft, Supervision, Formal analysis. **Neil Bricklebank:** Writing – review & editing, Writing – original draft, Supervision, Project administration, Conceptualization.

Declaration of competing interest

None.

Data availability

Data will be made available on request.

References

[1] L. Ao, Y-W. Yang, Coord. Chem. Rev. 530 (2025) 216488, https://doi.org/10.1016/j.ccr.2025.216488.
[2] G. Cavallo, P. Metrangolo, R. Milani, T. Pilati, A. Priimagi, G. Resnati, G. Terraneo, Chem. Rev. 116 (2016) 2478–2601.
[3] W.T. Pennington, T.W. Hanks, H.D. Arman, Struct. Bond. (Berlin) 126 (2008) 65–104.
[4] E. Adeniyi, F.E. Odubo, M. Zellerm, Y.V. Torubaev, S.V. Rosokha, Inorg. Chem. 62 (2023) 18239–18247.
[5] A. Guerriero, M. Peruzzini, L. Gonsalvi, Coord. Chem. Rev. 355 (2018) 328–361.
[6] J. Bravo, S. Bolaño, L. Gonsalvi, M. Peruzzini, Coord. Chem. Rev. 254 (2010) 555–607.
[7] A.D. Phillips, L. Gonsalvi, A. Romerosa, F. Vizza, M. Peruzzini, Coord. Chem. Rev. 248 (2004) 955–993.
[8] A. Guerriero, L. Gonslavi, Inorg. Chim. Acta. 572 (2024) 122295.
[9] F. Scalambra, P. Lorenzo-Luis, I. de los Rois, A. Romerosa, Eur. J. Inorg. Chem. (2019) 1529–1538.
[10] S.W. Jaros, U. Sliwinska-Hill, A. Bialonska, D.S. Nesterov, K. Kuropka, J. Sokolnicki, B. Bazanow, P. Smoleński, Dalton Trans. 48 (2019) 1123–11249.
[11] S.W. Jaros, M.F.C.Guedes da Silva P.Smoleński, M. Florek, J. Król, Z. Staroniewicz, A.J.L. Pombeiro, A.M. Kirillov, CrystEngCommun 15 (2013) 8060–8064.
[12] A.M. Kirillov, S.W. Wieczorek, A. Lis, M.F.C. Guedes da Silva, M. Florek, J. Król, Z. P.Smoleński, A.J.L Pombeiro, Cryst. Growth Des. 11 (2011) 271–2716.
[13] S.W. Jaros, M.F.C. Guedes da Silva, J. Król, M.C. Oliveira, A.J.L Pombeiro P. Smoleński, A.M. Kirillov, Inorg. Chem. 55 (2016) 1486–1496.
[14] S.W. Jaros, M. Florek, B. Bażanów, J. Panek, A. Krigul-Sobczak, M.C. Oliveira, J. Król, U. Silwińska-Hill, D.S. Nesterov, A.M. Kirillov, P. Smoleński, ACS App. Mater. Interfaces 16 (2024) 13411–13421.
[15] S.W. Jaros, J. Sokolnicki, M. Siczek, P. Smoleński, Inorg. Chem. 62 (2023) 19898–19907.
[16] A. Guerriero, A. Ienco, T. Hicks, A. Cilibrizzi, RSC Adv. 14 (2024) 21139–21150.
[17] B.J. Frost, W-C. Lee, K. Pal, T.H. Kim, D. VanDerveer, D. Rabinoih, Polyhedron 29 (2010) 2373–2380.
[18] A. García-Fernández, J. Díez, M.P. Gamasa, E. Lastra, Inorg. Chem. 48 (2009) 2471–2481.
[19] C. Apperley, N. Bricklebank, S.L. Burns, D.E. Hibbs, M.B. Hursthouse, K.M. A. Malik, J. Chem. Soc. Dalton Trans. (1998) 1289–1292.
[20] W.I. Cross, S.M. Godfrey, S.L. Jackson, C.A. McAuliffe, R.G. Pritchard, J. Chem. Soc. Dalton Trans. (1999) 2225–2230.
[21] W.-W. du Mont, M. Bätcher, C. Daniliuc, F.A. Devillanova, C. Druckenbrodt, J. Jeske, P.G. Jones, V. Lippolis, F. Ruthe, E. Seppälä, Eur. J. Inorg. Chem. (2008) 456–4577.
[22] W-W. du Mont, A. Martens-von Salzen, F. Ruthe, E. Seppala, G. Mugesh, F. A. Devillanova, V. Lippolis, N. Kuhn, J. Organomet. Chem. 623 (2001) 14–28.
[23] E. Seppälä, F. Ruthe, J. Jeske, W.-W. du Mont, P.G. Jones, Chem. Commun. (1999) 1471–1472.
[24] M. Arca, F. Demartin, F.A. Devillanova, A. Garau, F. Isaia, V. Lippolis, G. Verani, J. Chem. Soc. Dalton Trans. (1999) 3069–3073.
[25] K.H. Jogun, J.J. Stezowski, E. Fluck, J. Weidlein, Phosphorus Sulfur 4 (1978) 199–204.
[26] CrysAlisPro Software System, Rigaku Oxford Diffraction, 2018.
[27] G.M. Sheldrick, Acta Cryst. A71 (2015) 3–8.
[28] G.M. Sheldrick, Acta Cryst. C27 (2015) 3–8.
[29] O.V. Dolomanov, L.J. Bourhis, R.J. Gildea, J.A.K. Howard, H. Puschmann, J. Appl. Cryst. 42 (2009) 339–341.
[30] J.P. Perdew, M. Ernzerhof, K. Burke, Phys, Rev. Lett. 77 (1996) 3865–3868.
[31] J.P. Perdew, M. Ernzerhof, K. Burke, J. Chem. Phys. 105 (1996) 9982–9985.
[32] C. Adamo, V. Barone, J. Chem. Phys. 110 (1999) 6158–6170.
[33] F. Weingrad, R. Aldrichs, Phys. Chem. Chem. Phys. 7 (2005) 3297–3305.
[34] A. Schaefer, H. Horn, R. Aldrichs, J. Chem. Phys. 97 (1992) 2571–2577.
[35] S. Grimme, S. Ehrlich, L. Goerigk, J. Comput. Chem. 32 (2011) 1456–1465.
[36] F. Neese, WileyInterdiscip. Rev. 12 (2022) e1606, https://doi.org/10.1002/wcms.1606.
[37] A.V. Marenich, C.J. Cramer, D.G. Truhlar, Phys. Chem. B 113 (2009) 6378–6396.
[38] N. Mardirossian, M. Head-Gordon, J. Chem. Phys. 144 (2016) 214110.
[39] A.R. Allouche, J. Comput. Chem. 32 (2011) 174–182.
[40] M. Hanwell, D.E. Curtis, D.C. Lonie, T. Vandermeersch, E. Zurek, G.R. Hutchison, J. Cheminform. 4 (2012) 17.
[41] T. Lu, F. Chen, J. Comput. Chem. 33 (2012) 580–592.
[42] M. Casanoca-Paez, M.B. Dardis, L. Goerigk, J. Chem. Theory Comput. 15 (2019) 4735–4744.
[43] W.B. Schneider, G. Bistoni, M. Sparta, M. Saitow, C. Riplinger, A.A. Auer, F. Neese, J. Chem. Theory. Comput. 12 (2016) 4778–4792.
[44] C. Riplinger, P. Pinski, U. Becker, E.F. Valeev, F. Neese, Chem. Phys. 144 (2016) 024109.
[45] R.P. Lang, J. Am. Chem. Soc. 84 (1962) 1185–1192.
[46] C.C. Robertson, R.N. Perutz, L. Brammer, C.A. Hunter, Chem. Sci. 5 (2014) 4179–4183.
[47] Z. Khouba, T. Benabdallah, U. Maschke, Spectrochim. Acta A 125 (2014) 61–66.
[48] C. Laurence, J. Graton, M. Berthelot, M.J. El Ghomari, Chem. Eur. J. 17 (2011) 10431–10444.
[49] H. Pritzkow, Acta Crystallogr. B 31 (1975) 1589–1593.
[50] I.L. Karle, J. Chem. Phys. 23 (1955) 1793.
[51] U. Buontempo, A. Di Cicco, A. Filipponi, M. Nardone, P. Postorino, J. Chem. Phys. 107 (1997) 5720–5726.
[52] F. Bigoli, P. Deplano, M.L. Mercuri, M.A. Pellinghelli, A. Sabatini, E.F. Trogu, A. Vacca, J. Chem. Soc, Dalton Trans. (1996) 3583–3598.
[53] S.N. Steinmann, C. Piemontesi, A. Delachat, C. Corminboeuf, J. Chem. Theory. Compu. 8 (2012) 1629–1640.
[54] J.G. Hill, X. Hu, Chem. Eur. J. 19 (2013) 3620–3628.
[55] E.R. Johnson, S. Keinan, P. Mori-Sánchez, J. Contreras-García, A.J. Cohen, W. Yang, J. Am. Chem. Soc. 132 (2010) 6498–6506.
[56] M.A. Spackman, D. Jayatilaka, CrystEngComm 11 (2009) 19–32.
[57] J.J. Mckinnon, M.A. Spackman, D. Jayatilaka, Chem. Commun. (2007) 3814–3816.
[58] J-J. Zeng, Z-X. Wanga, F-G. Wu, J. Mater. Chem. B. 13 (2025) 8583–8597.